Radiation monitor extension for CMOS imaging instruments in nanosatellites

Josua Florczak, Tom Neubert, Egon Zimmermann, Heinz Rongen,
Martin Kaufmann, Friedhelm Olschewski, Stefan van Waasen

***Abstract*—This paper describes a low-cost extension for an imaging observation instrument as a radiation monitor. Adapted image processing methods enable discrimination between measured data and sensor / radiation-specific hazards and drives mitigation techniques to improve mission lifetime.**

Index Terms— **CMOS, CubeSat, dynamic threshold, low-cost, mitigation, radiation monitor, SAA**

I. Introduction

Nanosatellites have evolved over the past 20 years and are no longer just demonstration platforms; they are also used for scientific applications. Remote sensing instruments as part of observation units are typically launched in low earth orbits (LEO) to provide global coverage [1]. Realized with large pixel arrays, imaging capabilities are combined with spectrometer techniques to measure structures and temperatures with high spatial resolution. Current remote sensing applications [2] use scientific complementary metal oxide semiconductor (sCMOS) image sensors characterized by high signal-to-noise ratios, highly integrated readout electronics and low-cost procurement.

Depending on the orbit, there are different radiation environments with low radiation dose rates in equatorial and higher in polar orbits due to galactic cosmic rays (GCR), trapped protons and electrons. The polar orbits require careful radiation protection and safety margins in design requirements, e.g. if the South Atlantic Anomaly (SAA) is passed [3, 4]. Using particle detection to respond to unexpected events such as geomagnetic storms, an inhomogeneous or anisotropic radiation environment can help simplify design strategies that use essential mitigation measures without additional margin in shielding, saving design costs and testing steps. In addition, mitigation techniques such as triggering protection circuits during heavy radiation fluxes may be possible.

Customized CMOS image sensors or Monolithic Active Pixel Sensors (MAPS) have been used as particle detectors at CERN [5] and in space [6, 7]. However, such additional hardware solutions are not suitable for nanosatellites due to their additional mass, size, power consumption and cost.

In this paper, we extend the functionality of a commercial off the shelf (COTS) imaging CMOS sensor to include the ability to detect particles sufficiently well to determine the real radiation environment behind the shielding. The sensor is located in a spatial heterodyne interferometer (SHI) launched in December 2018 to derive atmospheric temperature profiles. This low cost radiation monitor solution provides an extension to react against unexpected events and enables additional mitigation techniques on the satellite electronics without the need to invest in additional hardware, mass, and size.

II. Design Materials and Methods

The methodological challenge in this integrated solution approach is to distinguish between the original measurement data and the radiation artifacts, since the measurement scene is continuously changing due to variations in the position control system and stray light conditions, as well as degradation effects of the sensor itself.

A. Instrument overview

A highly miniaturized limb sounder suited for nano/micro satellite constellations developed at Forschungszentrum Jülich (FZ Jülich) utilizes a monolithic SHI for atmospheric temperature sounding [2]. It is a fully integrated remote sensing instrument with optics, focal plane array, electronics, case construction, see Fig. 1. The instrument with the name AtmoSHINE operates as a secondary payload on a Chinese technology demonstration satellite, which was launched in December 2018. It is mounted on the shadow side of the satellite and measures the nighttime atmosphere from a sun synchronic orbit (SSO) of around 1000 km altitude.

The instrument contains a HWK1910A sCMOS sensor from Fairschield (BAE Systems) with a dimension of 5.04 µm × 5.04 µm and a total resolution of 1160 x 1976 pixels [8]. The sensor is located close to the readout electronics and is shielded with 6 mm aluminum including the satellite structure. AtmoSHINE has measured over a 10-month period since December 2018 in a timeshare with other instruments. During the observation periods, the instrument passes up to 14 times per day the SAA region. A typical limb image (level-0 data) in SAA region is shown in Fig. 2. The image shows the O_2 A-band nightglow layer, which peaks at an altitude of about 95 km, along with the radiation artefacts.

B. Artefact Segmentation

Artifacts are pixels that disturb the atmospheric measurement data caused by sensor characteristics and radiation environment. A two-step approach based on an adapted dynamic threshold (ADT) is used to segment these artifacts. For the first step, a method is implemented to segment the sensor-specific artefacts, such as more sensitive, dead or flickering single pixels, related to production processes and degradation effects.

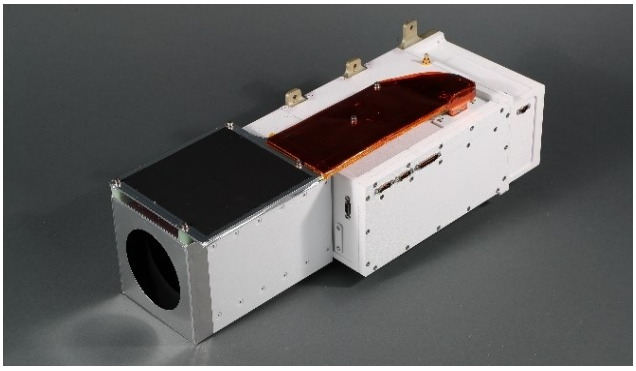

Fig. 1. AtmoSHINE flight model, a 3U miniaturized Spatial Heterodyne Interferometer (SHI) launched as secondary payload in December 2018. The sCMOS imaging sensor is placed orthogonal to the viewing direction of the instrument.

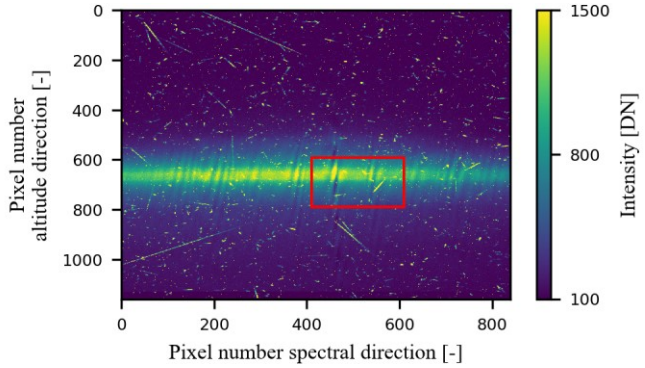

Fig. 2. Disturbed interferogram of the O_2 A-band nighttime limb emission by ionizing radiation as measured by the AtmoSHINE instrument on 7th August 2019 inside the SAA at 8°S, 100°W. The coordinates are pixel numbers. The vertical dimension is tangent altitude, covering approximately 60-120 km. The red highlighted subframe is used for algorithm verification.

The second step involves separation of radiation specific artefacts represented by variants of particle tracks, the number is counted and associated with an integral particle flux.

1) *Sensor artefacts*

For the segmentation of bad pixels, there exist a number of measurement and analysis procedures [9]. The "Interframe Statistics Median Filtering Detection" (ISMFD) described by [10] is such a segmentation algorithm that can detect flickering pixels in a measurement scene by using different exposure levels. An adapted method was developed, which does not require different exposure levels by analyzing sensitivity variations. This method uses the relative gain matrix

$$r_p(i,j) = g_p(i,j)/\breve{f}_p(i,j) \ , \tag{1}$$

where $g_p(i,j)$ is an original image p, as shown, e.g. in Fig. 2, and $\breve{f}_p(i,j)$ is the median image containing the median intensity by the direct neighbors. The lines and columns are identified with i and j. A single frame bad pixel matrix

$$N_p(i,j) = \begin{cases} 1 \text{ if } r_p(i,j) > r_{th} \\ 0 \text{ else} \end{cases} \quad \text{with} \quad r_{th} = 1 + 3\,\sigma \ , \tag{2}$$

can now be calculated depending on a dynamic threshold value r_{th} where σ describes the standard deviation related to the relative gain matrix $r_p(i,j)$.

To consider time variant artefacts, e.g. flickering pixels, the overall bad pixel matrix

$$R(i,j) = \begin{cases} 1 \text{ if } \sum_{p=1}^{Q} N_p(i,j) \geq \alpha(r_{th}) \\ 0 \text{ else} \end{cases} \tag{3}$$

is used which depends on the frame by frame probability threshold $\alpha(r_{th})$ where Q is the total number of frames. The value $\alpha(r_{th})$ is set to a threshold probability where the average number of pixels per single frame bad pixel matrix is close to the number of definitely bad pixels.

2) *Radiation artefacts*

Radiation-specific artifacts are clusters of pixels affected by ionizing particles that cross the epilayer of the sensor. The intensity and shape of these particle tracks depends on the particle type, its energy, and the angle of impact on the sensor surface [7]. For this artefact segmentation common frame-based algorithms exist, e.g. Detect and Remove Cosmic Rays (DCR) and Laplacian cosmic-ray rejection (L.A.Cosmic) [11].

Here, an adapted dynamic threshold method was used to focus on a limited parameter space and sufficient shape preservation of particle tracks due to the limited processing and memory capacities in nanosatellites. For this, a median $\widetilde{m_p}(i)$ is calculated for each frame p and line i of the images $g_p(i,j)$. Please note that the horizontal index j represents the interferogram.

With the parameter $\beta = 2$ estimated by detector response, exposure time and atmospheric signal variance, a dynamic threshold is calculated. In this way, we obtain a map

$$D_p(i,j) = \begin{cases} 1 \text{ if } g_p(i,j) > \beta * \widetilde{m_p}(i) \\ 0 \text{ else} \end{cases}, \tag{4}$$

of detected radiation-specific artifacts for each image and pixel, that allows to segment a pixel which is disturbed by ionization.

Finally, the detected artifacts were clustered with their direct neighbors and sensor-specific artefacts eliminated applying the bad pixel matrix $R(i,j)$. This enabled us to count the particle tracks and to obtain the integral particle flux.

III. Results

In order to compare the ADT algorithm with common cosmic ray detection algorithms, e.g. DCR and L.A.Cosmic., reference data from an in-orbit Space Application of Timepix Radiation Monitor (SATRAM) [7] were used. For this purpose, dark images with particle tracks from SATRAM database [12] were merged with an undisturbed interferogram image from the AtmoSHINE instrument. SATRAM uses a similar sensor technology and provides data from an orbit close to that of AtmoSHINE. These images were categorized into weak,

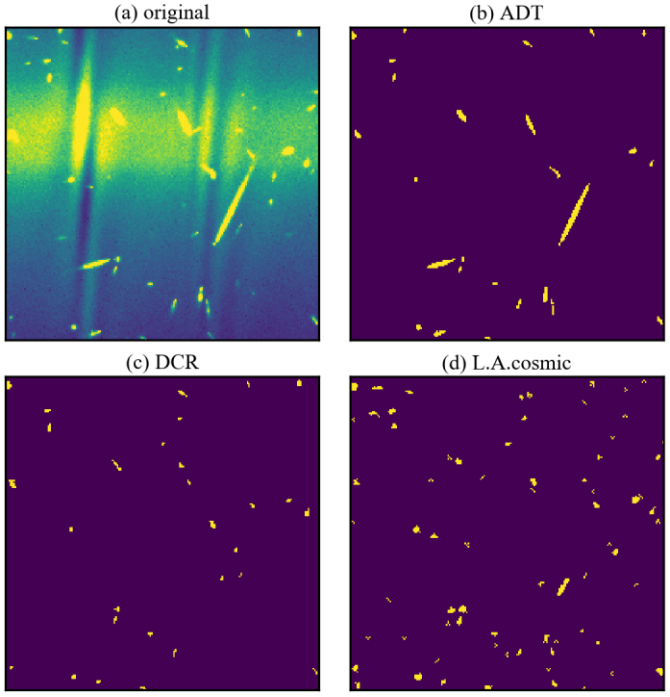

Fig. 3. Comparison of various cosmic ray detection algorithms using region of interest by 200x200 pixels, highlighted in red in Fig. 2. The original disturbed interferogram (a) contains intensities between 100DN and 1500DN. Discriminated results are shown using ADT (b), DCR (c) and L.A.Cosmic (d) method with yellow pixels marking the artifacts.

medium and heavy conditions and can contain particle tracks up to 20% of the sensor array. In Table I, the average relative deviations of the integral particle flux referenced to SATRAM data are listed, as well as their relative standard deviations.

All investigated detection algorithms show similar results for medium particle flux disturbances which will be quite common during mission lifetime, were the L.A.Cosmic is also accurate for heavy and DCR especially for weakly affected images. In contrast, the presented ADT method fulfills all three conditions within uncertainties in particle flux below 6% deviation from the SATRAM instrument. This enables procedures to unexpected events like geomagnetic storms, and inhomogeneous or anisotropic radiation environment conditions. A major advantage of ADT against DCR and L.A.Cosmic is its good structure preservation of particle tracks which we can see by an example in Fig. 3. The figure shows a 200x200 pixel subimage of a weakly to medium affected image from the middle position of the sensor in (a) and the corresponding detection results. In (d) the flux by L.A.Cosmic is overestimated in accordance with Table I. The form of the particle tracks differ in (c) and (d), which may be caused by the missing optimization of the parameters as well as the focus of these cosmic ray detection algorithms is on correcting affected pixels and not on segmenting particle tracks. The ADT algorithm provides the different types of particle tracks, as shown in (b) and is suitable for further analysis, e.g., calculation of linear energy transfer (LET) as a parameter to determine single event upset (SEU) rates.

TABLE I
RELATIVE ERROR OF SEVERAL PARTICLE DETECTION ALGORTIHMS

Disturbance [%]	0-2.5 (weak)	2.5-10 (medium)	10-20 (heavy)
Detection algorithm	Particle flux deviation [%]	Particle flux deviation [%]	Particle flux deviation [%]
ADT	-1 ± 3	-2.3 ± 3	1.5 ± 2
L.A.Cosmic	> 25 ± 25	1.6 ± 4	-3.9 ± 2
DCR	-7 ± 10	-1.5 ± 4	< -25 ± 25

A. *Observed integral particle flux*

During observation on 7th August 2019, particle fluxes were acquired using a region of interest of 840x1160 pixels for day and nighttime with a total of 2072 measurements. Each acquired image of the AtmoSHINE instrument was analyzed and bad pixels were removed according to section II.B. These images were taken with the CMOS sensor inside the instrument, and the results imply the effective shielding of the satellite. The integral particle flux is plotted in Fig. 4a for the location of the satellite and varies about three orders of magnitude in this period, with the highest values when passing the SAA region.

To verify these results, the flux of trapped protons and electrons were simulated with AP8 and AE8 model, solar particles with Xapsos and galactic cosmic rays with ISO-15390 model respectively using SPENVIS [13]. Fig. 4b shows the time distribution of integral particle flux according to the simulation and the measurement. The corresponding regions are labeled and show a suitable correlation in the SAA region. The difference in particle fluxes by an order of magnitude can be explained by daily fluctuations in particle fluxes [14], which

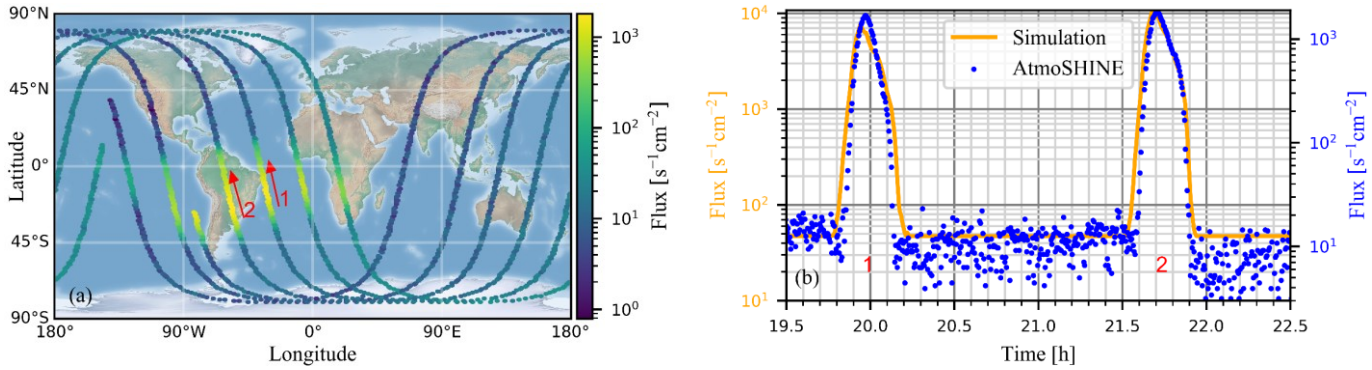

Fig. 4. Spatial (a) and time (b) distributions of integral particle flux measured by AtmoSHINE on 7th August 2019 at an altitude of 1073km. Data shown in (b) represents a 3h orbit path with two tracks across the SAA. Time distribution is compared with simulated integral particle flux including an equivalent Al shielding thickness of 6 mm. For orientation, the corresponding regions are labeled.

differ significantly from the long-term averaged values used in simulation, and by differences in effective shielding thickness.

B. Mitigation measures

As result of particle counting, additional mitigation measures can be identified. Implementing real-time monitoring to record the accumulated dose rates determine degradation defects in the sensor or detect bad pixels. Furthermore, adapted exposure times can improve the data quality depending on radiation environments. In addition, at a predefined particle flux threshold, it may be possible to protect the instrument by selectively switching sensitive components on and off. Investigations based on simulation data were performed by Neubert et al. [15] and results in a reduction of error rate due to SEUs in the electronics by a factor of four. This measure is coupled with a limitation in measurement time.

In Fig. 5 the shutdown time per orbit is plotted against the integral particle flux threshold on the x-axis, when the threshold level (red line) is used. Taking into account the deviations due to shielding, 8-9% less shutdown time is needed to obtain the same reliability of the instrument, which will correspond to an effective increase in measurement time of approx. 2 hours per day.

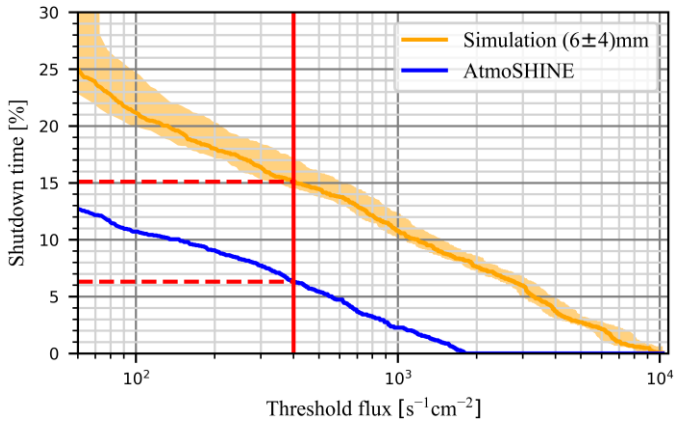

Fig. 5. Relative shutdown time for different threshold flux values on 7th August 2019. The difference in shutdown time between simulated (orange) and measured (blue) particle flux by short-term fluctuations is shown according for a given threshold line (red). Simulation results include an equivalent Al shielding thickness of 6mm and their margins.

IV. Conclusion

With the AtmoSHINE instrument the feasibility of a particle counter based on COTS sCMOS sensors could be demonstrated, which detects particle fluxes with an uncertainty only 6% higher than common particle counters by using an adapted dynamic threshold method (ADT). The presented method uses a two-step approach to detect sensor- and radiation-specific artifacts. Even with highly varying measurement scenes, this shows suitable results in the segmentation of individual particle tracks.

In the future, this will allow real-time detection of sensor degradation effects, setting demand-controlled exposure times to improve data quality, or implementing additional mitigation measures. It was shown that on radiation quiet days, count rates may well be up to an order of magnitude lower compared to simulation results, which opens up the possibility of responding much more directly to the effective radiation environment, for example by selectively switching off the instrument. This increases the lifetime and it has been shown that the measurement time can be extended up to 2 hours per day.

Further investigation is planned to determine the effective energies of the particles and so the LET spectra. This would allow a real-time analysis of the actual SEU error rates in order to operate the instrument with further mitigation measures even longer in orbit and to enable long-term observations.

References

[1] A. Poghosyan and A. Golkar, “CubeSat evolution: Analyzing CubeSat capabilities for conducting science missions,” *Prog. Aeronaut. Sci.*, vol. 88, pp. 59–83, Jan. 2017, doi: 10.1016/j.paerosci.2016.11.002.

[2] M. Kaufmann *et al.*, “A highly miniaturized satellite payload based on a spatial heterodyne spectrometer for atmospheric temperature measurements in the mesosphere and lower thermosphere,” *Atmos. Meas. Tech.*, vol. 11, no. 7, pp. 3861–3870, Jul. 2018, doi: 10.5194/amt-11-3861-2018.

[3] K. A. LaBel, A. H. Johnston, J. L. Barth, R. A. Reed, and C. E. Barnes, “Emerging radiation hardness assurance (RHA) issues: a NASA approach for space flight programs,” IEEE Trans. Nucl. Sci., vol. 45, no. 6, pp. 2727–2736, Dec. 1998, doi: 10.1109/23.736521.

[4] M. Campola, “Taking Smallsats to the Next Level - Sensible Radiation Requirements and Qualification That Won’t Break the Bank,” in Proc. AIAA/USU Conf. Small Satellites, 2018, p. 7.

[5] W. Snoeys, “CMOS monolithic active pixel sensors for high energy physics,” *Nucl. Instrum. Methods Phys. Res., Sect. A*, vol. 765, pp. 167–171, Nov. 2014, doi: 10.1016/j.nima.2014.07.017.

[6] E. F. Mitchell *et al.*, “The Highly Miniaturised Radiation Monitor,” J. Instrum., vol. 9, no. 07, pp. P07010–P07010, Jul. 2014, doi: 10.1088/1748-0221/9/07/p07010.

[7] C. Granja *et al.*, “The SATRAM Timepix spacecraft payload in open space on board the Proba-V satellite for wide range radiation monitoring in LEO orbit,” *Planet. Space Sci.*, vol. 125, pp. 114–129, Jun. 2016, doi: 10.1016/j.pss.2016.03.009.

[8] J. Liu *et al.*, “Investigation on a SmallSat CMOS image sensor for atmospheric temperature measurement,” in ICSO 2018, Chania, Greece, Jul. 2019, vol. 11180, pp. 2384–2393, doi: 10.1117/12.2536157.

[9] W. Isoz, T. Svensson, and I. Renhorn, “Nonuniformity correction of infrared focal plane arrays,” in Infrared Technol. Appl. XXXI, Orlando, Florida, USA, May 2005, vol. 5783, pp. 949–960, doi: 10.1117/12.606691.

[10] Yang Cao, Weiqi Jin, Chongliang Liu, and Xiu Liu, “Scene-based bad pixel dynamic correction and evaluation for IRFPA device,” in *Adv. OptoElectron and Micro/nano-optics*, Guangzhou, China, Dec. 2010, pp. 1–4, doi: 10.1109/AOM.2010.5713516.

[11] C. L. Farage and K. A. Pimbblet, “Evaluation of Cosmic Ray Rejection Algorithms on Single-Shot Exposures,” *Publ. Astron. Soc. Aust*, vol. 22, no. 3, pp. 249–256, 2005, doi: 10.1071/AS05012.

[12] SATRAM dataset, “SATRAM/Timepix visualization,“ H. Waage and CTU Prague, Apr. 2021. [Online]. Available: https://satram.utef.cvut.cz/.

[13] S. Calders *et al.*, “Modeling the space environment and its effects on spacecraft and astronauts using SPENVIS,” presented at the 15th Int. Conf. Space Oper., Marseille, France, May 2018, doi: 10.2514/6.2018-2598.

[14] C. Granja and S. Polansky, “Mapping the space radiation environment in LEO orbit by the SATRAM Timepix payload on board the Proba-V satellite,” AIP Conf. Proc., vol. 1753, no. 1, p. 080006, 2016, doi: 10.1063/1.4955376.

[15] T. Neubert *et al.*, “System-on-module-based long-life electronics for remote sensing imaging with CubeSats in low-earth-orbits,” *J. Appl. Rem. Sens.*, vol. 13, no. 03, p. 032507, Jul. 2019, doi: 10.1117/1.JRS.13.032507.